Available online at www.sciencedirect.com
ScienceDirect
Journal of Power Sources 176 (2008) 62–69
JOURNAL OF POWER SOURCES
www.elsevier.com/locate/jpowsour

Fabrication and characterization of metal-supported solid oxide fuel cells

Changbo Lee, Joongmyeon Bae *

Department of Mechanical Engineering, Korea Advanced Institute of Science and Technology, 373-1 Guseong-Dong, Yuseong-Gu, Daejeon 305-701, Republic of Korea

Received 19 July 2007; received in revised form 17 September 2007; accepted 4 October 2007
Available online 30 October 2007

Abstract

Metal-supported solid oxide fuel cells (SOFCs) are an acceptable approach to solving the serious problems of SOFC technology, such as sealing and mechanical strength. In this work, commercial stainless-steel plates, STS430, are used as supporting bodies for a metal-supported SOFC in order to decrease the number of fabrication steps. The metal support for a single-cell has a diameter of 28 mm, a thickness of 1 mm, and a channel width of 0.4 mm. A thin ceramic layer, composed of yttria-stabilized zirconia (YSZ) and NiO/YSZ, is attached to the metal support by using a cermet adhesive. $La_{0.8}Sr_{0.2}Co_{0.4}Mn_{0.6}O_3$ perovskite oxide serves as the cathode material because of its low impedance on the YSZ electrolyte, according to half-cell tests. The maximum power density of the cell is 0.09 W cm^{-2} at 800 °C. The effects of temperature, oxygen partial pressure, and current collection by pastes are investigated. The oxygen reduction reaction at the cathode dominates the overall cell performance, according to experimental and numerical analyses.

Keywords: Metal-supported solid oxide fuel cells; Cathode; Joining process; Oxygen reduction reaction; In situ sintering; Power density

1. Introduction

Metallic interconnects are commonly used in the stack fabrication of planar-type, ceramic-supported, solid oxide fuel cells (SOFCs) to reduce the operating temperature to below 700 °C. The most important technical challenges of commercial ceramic-supported SOFC stacks are sealing and mechanical strength. The efficiencies of fabrication and operation cannot be improved without solving these issues. Several research groups have developed metal-supported SOFCs in order to address these problems. Ceres Power Ltd. and Imperial College developed a low-temperature metal-supported SOFC with a maximum power density of 0.4 W cm^{-2} at 570 °C and fabricated a stack of 140 W output with 40 cells that is approaching commercial use [1–3].

In this study, metal-supported SOFC single-cells with a new structure are fabricated and characterized by using a galvanodynamic test, impedance analysis, and numerical analysis. The ceramic component is attached to the mechanically processed metal support by using a cermet adhesive to reduce the fabrication costs.

2. Experimental

$La_{0.8}Sr_{0.2}Co_{1-x}Mn_xO_{3-\delta}$ (LSCM) ($x = 0$, 0.2, 0.5, 0.6, 0.8, and 1) was prepared by the glycine nitrate process (GNP). The chemical formula is abbreviated using the first letters of the chemical symbol to represent the material composition and is followed by the molar ratio with hyphen. For example, $La_{0.8}Sr_{0.2}MnO_{3-\delta}$ is expressed as LSM-82, and $La_{0.8}Sr_{0.2}Co_{0.5}Mn_{0.5}O_{3-\delta}$ is expressed as LSCM-8255. The desired molar compositions of the selected nitrates were mixed with glycine and de-ionized water. Then, the aqueous solution was heated with stirring, until a powder formed on combustion. The powders were calcined at 1000 °C for 1 h to effect conversion to the crystal phase. 8 mol% yttria-stabilized zirconia (YSZ) electrolyte pellets were prepared from YSZ fine powder (Tosoh TZ-8Y). The powder was uniaxially pressed in a circular mold at 2 MPa. The resultant green pellets were sintered at 1500 °C for 4 h. Dense YSZ pellets, with approximate dimensions of 26 mm diameter and 2 mm thickness, were obtained. The pellets were

* Corresponding author. Tel.: +82 42 869 3045; fax: +82 42 869 8207.
E-mail addresses: leecb@kaist.ac.kr (C. Lee), jmbae@kaist.ac.kr (J. Bae).

0378-7753/$ – see front matter © 2007 Elsevier B.V. All rights reserved.
doi:10.1016/j.jpowsour.2007.10.067

Nomenclature

A	area (m^2)
C	concentration ($mol\,m^{-3}$)
d	diameter (m)
D	diffusion coefficient ($m^2\,s^{-1}$)
E	activation energy (eV)
F	Faraday constant (96,485 $C\,mol^{-1}$)
g	Gibbs free energy ($J\,mol^{-1}$)
i	current density ($A\,m^{-2}$)
i_0	exchange current density ($A\,m^{-2}$)
J	molar flux ($mol\,m^{-2}\,s^{-1}$)
$\bar{k}$	Boltzmann constant ($8.62 \times 10^{-5}\,eV\,K^{-1}$)
Kn	Knudsen number, $\lambda/d_{p,avg}$
l	thickness (m)
m	reaction order
M	molecular weight ($kg\,mol^{-1}$)
n	electron number participating in reaction
P	pressure (Pa)
R	area specific resistance ($\Omega\,m^2$)
R_0	pre-exponent constant (balanced unit)
R_Ω	resistance (Ω)
$\bar{R}$	universal gas constant ($8.314\,J\,mol^{-1}\,K^{-1}$)
T	temperature (K)
v	Fuller diffusion volume (balanced unit)
V	voltage (V)
x	mole fraction

Greek symbols

β	symmetry factor
ε	porosity
η	polarization loss (V)
σ	electrical conductivity ($S\,m^{-1}$)
σ_0	pre-exponent constant (balanced unit)
τ	tortuosity

Superscripts

m	reaction order
r	reaction site
0	standard condition

Subscripts

a	anode or anodic
act	activation
avg	average
c	cathode or cathodic
conc	concentration
e	electrolyte
eff	effective
H_2	hydrogen
H_2O	water vapour
i	species
in	internal
j	species
Kn	Knudsen
m	metal
M	medium
N_2	nitrogen
oc	open-circuit
ohm	ohm
O_2	oxygen
p	pore
tot	total

cleaned with hydrofluoric acid for 1 min prior to cathode coating to remove siliceous material because SiO_2 in raw YSZ pellets can block electrical conduction paths or reaction sites [4].

The cathode materials were circularly screen-printed, with a 10 mm diameter, in the centre of both sides of the YSZ pellets. Sintering was carried out at 1200 °C for 1 h, producing symmetrical half-cells. The impedance was measured for each sample at 100 °C intervals from 500 to 900 °C in air. A half-cell with a cathode that was dried at 200 °C, but not sintered at 1200 °C, was prepared to observe the cathode sintering effect. The impedance of the sample was measured at 800 °C with in situ sintering of the cathode during the measurement. The area specific resistance (ASR) values of the cathode were calculated by considering half-cell symmetry (Eq. (1))

$$R_c = \frac{R_\Omega}{2} A_c \tag{1}$$

The ceramic component composed of the electrolyte and anode was fabricated by a tape-casting process. The electrolyte was YSZ and the anode was a compound of NiO and YSZ at a weight ratio of 6:4. Slurries for the tape-casting method were prepared by ball-milling for 48 h. The compositions of the slurries were 15 wt.% binder (Butvar B-98), 2 wt.% dispersant (polyvinylpyrrolidone), 10 wt.% plasticizer (polyethyleneglycol), and 100 wt.% solvent (lab-made S-NECS) compared with the weights of the ceramic powders. The ball-milled slurries were degassed in a vacuum desiccator to minimize any fabrication defects. Ceramic films were obtained by pulling the slurry with a tape caster with 150 or 250 μm height. Green bodies containing the electrolyte and anode were prepared by stacking several sheets of the ceramic films. Thin ceramic layers of the dense electrolyte and an appropriate porous anode were fabricated by sintering at 1500 °C for 4 h in air.

STS430, a ferritic stainless-steel, which had a diameter of 28 mm and a thickness of 1 mm was used as the metal support. A zigzag-shaped long hole with a width of 0.4 mm was bored through the metal support by a wire cutting process to create a flow channel. The cermet adhesive paste was made from 80 wt.% ferritic AISI410 powder and 20 wt.% NiO/YSZ powder. The thin ceramic layer was placed on the metal support which was covered with the cermet adhesive. This combined body was sintered at 1400 °C for 10 h to achieve good adhesion at the interface. LSCM-8246 was screen-printed on the sintered body and dried at 200 °C. The cathode was sintered in situ because the cell is easily oxidized in air at temperatures above 800 °C. The con-

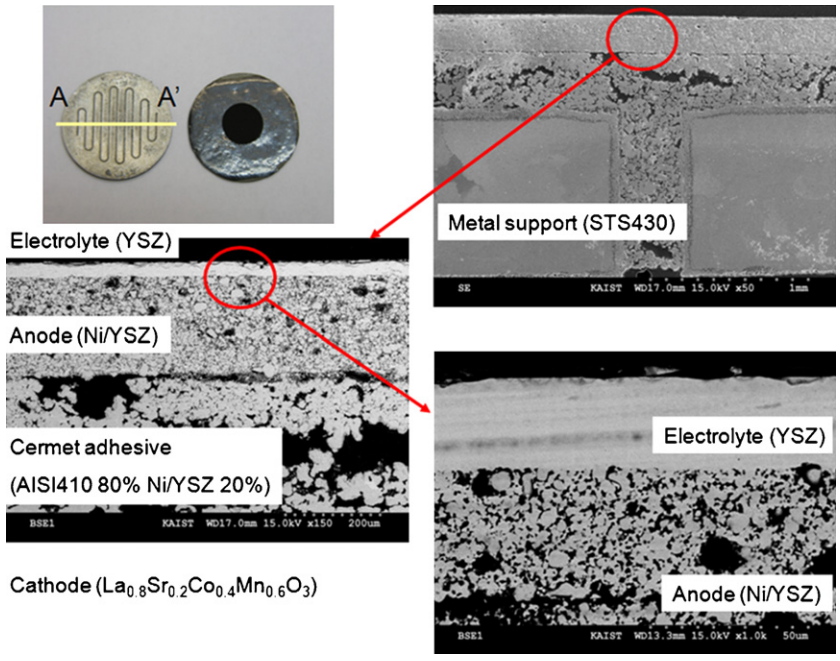

Fig. 1. Single-cell structure of metal-supported SOFC (photograph: overall single-cell shape, SEM images: cross-sectional view from A to A′).

figuration of the metal-supported SOFC single-cell is shown in Fig. 1.

A single-cell test set-up was prepared with reference to previous studies [5,6]. Hydrogen and air were supplied at the same flow rate of 2.5×10^{-6} m^3 s^{-1}. Dry hydrogen was changed to 3 mol% humidified hydrogen by passing it through a bubbler filled with de-ionized water. The water content in the feed air was removed by using a chemical dehumidifier. Cell performance was measured by a galvano-dynamic method. The oxygen partial pressure dependence of the cell performance was investigated to determine the governing factors. Premixed gases with an oxygen partial pressure of 0.2 and 1 atm (balance nitrogen) were used.

3. Numerical

The open-circuit voltage (OCV) of a fuel cell can be calculated from the Nernst equation, i.e.,

$$V_{oc} = -\frac{\Delta g^0}{nF} + \frac{\bar{R}T}{nF} \ln \frac{P_{H_2} P_{O_2}^{0.5}}{P_{H_2O}} \tag{2}$$

Three irreversible polarization losses are enhanced with increasing current from the OCV state. The losses are classified as activation polarization, ohmic polarization, and concentration polarization. The Butler–Volmer equation is widely used for activation polarization loss, i.e.,

$$i = i_0 \left[\exp\left((1-\beta) \frac{nF\eta_{act}}{\bar{R}T} \right) - \exp\left(-\beta \frac{nF\eta_{act}}{\bar{R}T} \right) \right] \tag{3}$$

The symmetry factor (β) can be assumed to be 0.5 for general fuel cell applications [7,8]. The activation polarization losses for the anode and cathode can be rearranged, respectively, as follows:

$$\eta_{act,a} = \frac{2\bar{R}T}{nF} \sinh^{-1}\left(\frac{i}{2i_{0,a}} \right) \tag{4}$$

$$\eta_{act,c} = \frac{2\bar{R}T}{nF} \sinh^{-1}\left(\frac{i}{2i_{0,c}} \right) \tag{5}$$

Ohmic polarization losses are mostly occupied by the electrolyte and oxidized layer of metal support, i.e.,

$$\eta_{ohm} = \left(\frac{l_e}{\sigma_e} + R_m \right) i \tag{6}$$

The electrical conductivity of the electrolyte (σ_e) and resistivity of the oxidized layer of metal (R_m), with respect to temperature, obey the Arrhenius relation as follows:

$$\sigma_e = \frac{\sigma_0}{T} \exp\left(\frac{-E_{act,e}}{\bar{k}T} \right) \tag{7}$$

$$R_m = R_0 T \exp\left(\frac{E_{act,m}}{\bar{k}T} \right) \tag{8}$$

The coefficients for Eqs. (7) and (8), which were measured by half-cell tests, are shown in Table 1. The differences in the partial pressures of the reactants (H_2, O_2) and product (H_2O) between the reaction sites and channel inlet were determined by flow characteristics in the electrode structure, i.e.,

$$\eta_{conc,a} = -\frac{\bar{R}T}{nF} \ln\left(\frac{P_{H_2}^r P_{H_2O}}{P_{H_2} P_{H_2O}^r} \right) \tag{9}$$

$$\eta_{conc,c} = -\frac{\bar{R}T}{2nF} \ln\left(\frac{P_{O_2}^r}{P_{O_2}} \right) \tag{10}$$

The partial pressures at the reaction sites can be calculated by using Fick's steady-state diffusion and electrical current gen-

Table 1
Input data for numerical simulation of metal-supported solid oxide fuel cell

Parameters	Value
Temperature, T	800 °C
Hydrogen pressure, P_{H_2}	0.97 atm
Water vapour pressure, P_{H_2O}	0.03 atm
Oxygen pressure, P_{O_2}	0.21 atm
Exchange current density of anode, $i^0_{0,a}$	220 A m^{-2} [16,17]
Exchange current density of cathode, $i^0_{0,c}$	50 A m^{-2}
Pre-exponent coefficient, σ_0	$1.15 \times 10^8\ \Omega^{-1}\ m^{-1}\ K$
Pre-exponent coefficient, R_0	$9.59 \times 10^{-14}\ \Omega\ m^2\ K^{-1}$
Activation energy of YSZ electrolyte, $E_{act,e}$	0.98 eV
Activation energy of metal support, $E_{act,m}$	1.02 eV
Porosity of anode, ε_a	0.3 [8–10]
Porosity of cathode, ε_c	0.3 [8–10]
Tortuosity of anode, τ_a	3 [9,10]
Tortuosity of cathode, τ_c	3 [9,10]
Average pore diameter of anode, $d_{p,avg,a}$	1×10^{-6} m
Average pore diameter of cathode, $d_{p,avg,c}$	5×10^{-7} m
Reaction order of anode, m_a	1/2 [18]
Reaction order of cathode, m_c	3/8 [19]
Thickness of electrolyte, l_e	3×10^{-5} m
Thickness of anode and porous metal support, l_a	6×10^{-4} m
Thickness of cathode, l_c	5×10^{-5} m

eration as follows:

$$J_{H_2} = -D_{eff,a}\nabla C_{H_2} + x_{H_2}(J_{H_2} + J_{H_2O}) \quad (11)$$

$$J_{H_2O} = -D_{eff,a}\nabla C_{H_2O} + x_{H_2O}(J_{H_2} + J_{H_2O}) \quad (12)$$

$$J_{O_2} = -D_{eff,c}\nabla C_{O_2} + x_{O_2}(J_{O_2} + J_{N_2}) \quad (13)$$

$$J_{H_2} = -J_{H_2O} = 2J_{O_2} = \frac{i}{nF} \quad (14)$$

The sum of the fluxes of hydrogen and water vapour in the anode is zero and the flux of nitrogen in the cathode is presumably zero. The effective diffusivity of each species is generally calculated by considering both Knudsen diffusion and binary diffusion because these processes may be competitive according to circumstances in the electrode microstructure. It can be depicted as follows:

$$D_{eff,i} = \frac{\varepsilon_M}{\tau_M}\left(\frac{1}{D_{Kn,i}} + \frac{1}{D_{ij}}\right)^{-1} \quad (15)$$

Knudsen diffusivity [8–11] and binary diffusivity [12,13] were calculated as follows, respectively:

$$D_{Kn,i} = \frac{d_{p,avg}}{3}\sqrt{\frac{8\bar{R}T}{\pi M_i}} \quad (16)$$

$$D_{ij} = \frac{0.00143T^{1.75}}{M_{ij}^{1/2}\left(v_i^{1/3} + v_j^{1/3}\right)^2 P_{tot}} \quad (17)$$

Eq. (17) was proposed by Fuller [12] and has been widely used for SOFC modelling [9,10,14]. The effective diffusivities in the anode and cathode can be calculated as follows, respectively [8]:

$$D_{eff,a} = x_{H_2O} D_{eff,H_2} + x_{H_2} D_{eff,H_2O} \quad (18)$$

$$D_{eff,c} = D_{eff,O_2} \quad (19)$$

The theoretical cathode impedance at OCV can be calculated by differentiating Eq. (5) if the symmetry factor is 0.5, i.e.,

$$R_c = \frac{\bar{R}T}{nFi_{0,c}} \quad (20)$$

The exchange current density of the cathode was measured from impedance values through half-cell tests. Exchange current densities at each electrode, which are functions of pressure and temperature, were estimated from the Arrhenius relation [15]:

$$i_0 = i_0^0\left(\frac{P_i}{P_i^0}\right)^m \exp\left[-\frac{E_{act,i_0}}{\bar{R}}\left(\frac{1}{T} - \frac{1}{T^0}\right)\right] \quad (21)$$

The operational cell voltage was computed by considering the effects of internal electrical loss and/or gas tightness. Voltage loss from these effects was measured from experimental data, i.e.,

$$V = V_{oc} - \eta_{act,a} - \eta_{act,c} - \eta_{ohm} - \eta_{conc,a} - \eta_{conc,c} - \eta_{in} \quad (22)$$

Numerical calculations for the current–voltage (I–V) curve and polarization losses were carried out by the finite volume method (FVM). Numerical results were compared with experimental results to classify the main factors that influence the single-cell performance. The constants used are listed in Table 1 [8–10,16–19].

4. Results and discussion

4.1. Cathode property on YSZ electrolyte by half-cell testing

The ASR property of the LSCM cathode on the YSZ electrolyte was acquired as a function of temperature and composition (Fig. 2). The ASR initially decreases with increasing Co content because of the good oxygen reduction kinetics of the Co-containing perovskite oxide. However, the ASR then increases with increasing Co content after LSCM-8246. LSCM-8246 has

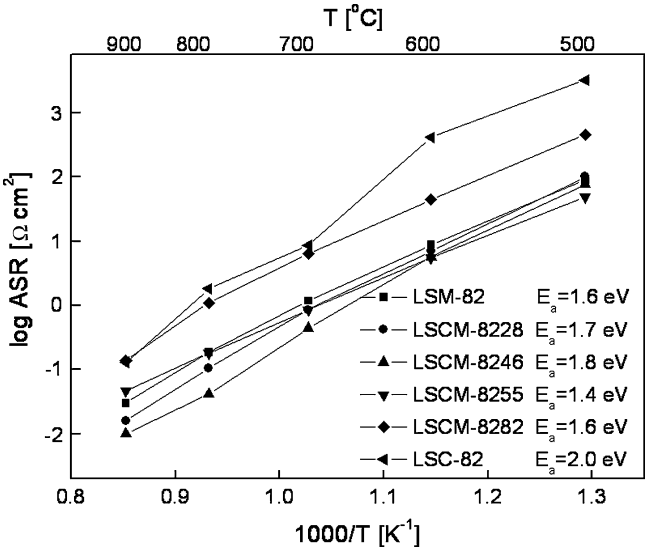

Fig. 2. Temperature dependence of ASR of LSCM cathodes on YSZ electrolyte.

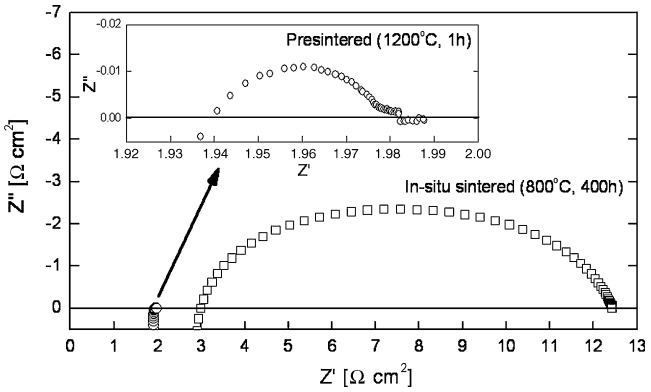

Fig. 3. Impedance spectra for non-sintered LSCM-8246 and pre-sintered LSCM-8246 on YSZ electrolyte at 800 °C.

the lowest impedance on YSZ electrolyte. This may be caused by competition among the reaction kinetics, thermal expansion compatibility, and chemical reactivity between the cathode and electrolyte [19].

The impedance of the cathode, which was previously sintered at 1200 °C for 1 h, is much lower than the impedance of the cathode sintered in situ at 800 °C for 400 h (Fig. 3). The ASR value of the cathode sintered at 1200 °C is 0.04 Ω cm^2, whereas that of the cathode sintered in situ at 800 °C is 9.4 Ω cm^2. The sintering phenomenon is strongly dependent on temperature because grain growth and densification is accomplished by the diffusion of cations. Adhesion is generally improved with a higher sintering temperature. Therefore, a cathode material with low impedance, even at conditions of in situ sintering, should be targeted.

4.2. Single-cell property

LSCM-8246 was used as the cathode for single-cell tests because of its low impedance on the YSZ electrolyte, despite the uncertainty of in situ sintering (Figs. 2 and 3). Current–voltage–power (*I–V–P*) curves at various temperatures are shown in Fig. 4. The maximum power densities at 700, 800, and 900 °C are 0.03, 0.09, and 0.18 W cm^{-2}, respectively. These

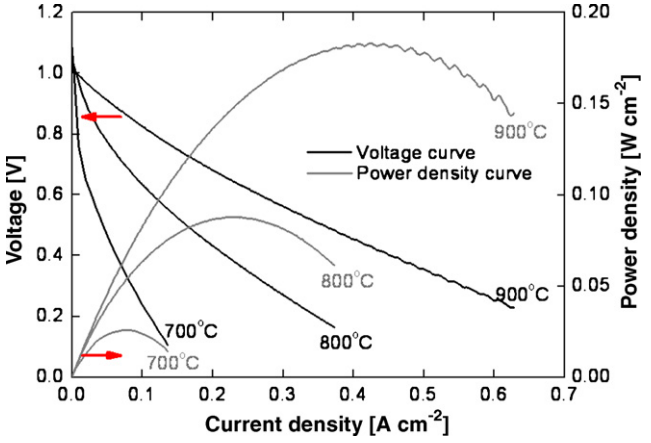

Fig. 4. *I–V–P* curves of single-cell of metal-supported SOFC at 700, 800 and 900 °C.

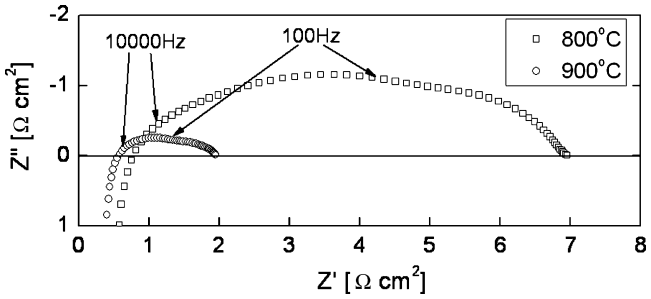

Fig. 5. Impedance spectra of single-cell of metal-supported SOFC at 800 and 900 °C.

power densities are low compared with a conventional ceramic SOFC. In situ sintering of the cathode may be a major cause for the low performance.

Impedances of the single-cells were measured at the OCV state to classify initially the governing factors (Fig. 5). The impedance of the single-cell shown in Fig. 5 is smaller than that of the half-cell shown in Fig. 3 at 800 °C. It is considered that the impedance results are in an acceptable error range because both impedances for the single-cell and half-cell are of the order of several ohms. There are possible explanations for the error. One hypothesis is the activation effect on the electrode by the applied current [20,21]. The half-cell test was always carried out at the OCV state; but the single-cell test must be in the condition of electrical conduction when measuring the current–voltage relationship. Electrical current in fuel cells may enhance electrode properties. Therefore, the impedance of the single-cell can be smaller than that of the half-cell. In addition, there are some further possibilities that might be considered, such as a different fabrication process and a cathode sintering effect.

Activation polarization and ohmic polarization decrease with increasing temperature because the polarizations obey thermally activated processes. The effect of bulk gas diffusion in the electrode is negligible because the impedances at low frequency (<1 Hz) are small. The frequency of the impedance for gas diffusion is known to be 0.1 Hz at a time constant of the low impedance semi-circle [19]. Note that the role of gas diffusion may not be important when no electrical current flows. The impedance in the low-frequency region (<1 Hz) can be increased even at the OCV state if the oxygen partial pressure is lower than that in air. Therefore, the electrochemical impedances imply the sum of the oxygen reduction reaction at the cathode and the hydrogen oxidation reaction at the anode. The ohmic resistance is 0.75 Ω cm^2 at 800 °C. This value consists of the electrolyte resistance, 0.1 Ω cm^2 (YSZ with 30 μm thickness), the oxidized layer resistance of the metal support, 0.15 Ω cm^2 [22], and the contact resistance, 0.5 Ω cm^2. The ohmic resistances of the electrodes are negligible because of the high electrical conductivities of the cathode (lanthanide-based perovskite oxides) and the anode (Ni/YSZ) at 10–1000 S cm^{-1} at 800 °C [23,24].

The cathode is covered with Pt paste and the metal support is covered with Ni paste to reduce the electrical contact resistance. The characteristics of the *I–V–P* curve and the impedance are improved by the use of these pastes (Figs. 6 and 7). The performance of the single-cell is enhanced twofold at 700 °C, with

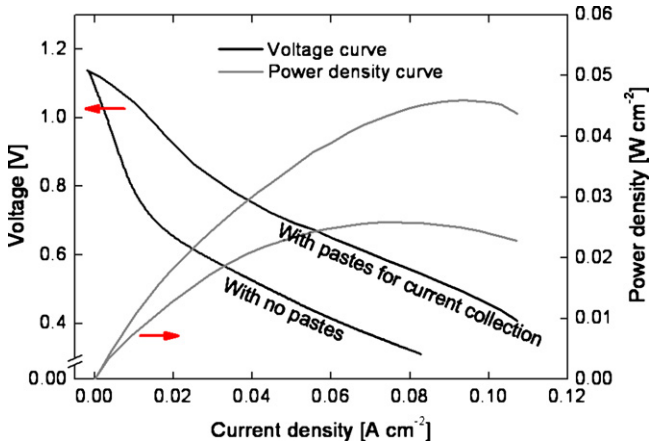

Fig. 6. *I–V–P* curves of single-cell with and without pastes for current collection at 700 °C (Pt paste on cathode and Ni paste on metal support).

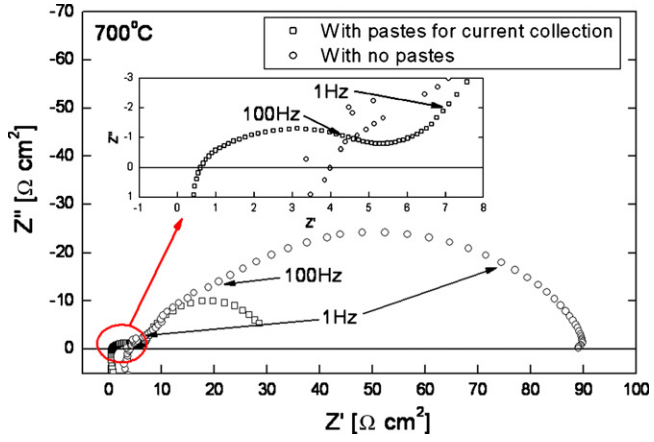

Fig. 7. Impedance spectra of single-cell with and without pastes for current collection at 700 °C (Pt paste on cathode and Ni paste on metal support).

respect to maximum power density, because of the increased electrically active area. The ohmic resistance of the single-cell is 0.65 Ω cm^2 at 700 °C (Fig. 7). The electrolyte resistance is 0.3 Ω cm^2 and the oxidized layer resistance of the metal support is 0.4 Ω cm^2 at 700 °C from the half-cell test [22]. It is noted that no contact resistance is displayed by the current collection method because the impedances of the single-cell and half-cell are equivalent.

Cell performance depends on oxygen partial pressure as well as temperature (Fig. 8). The measured OCV values of the single-cell are 1.01–1.04 V for the experimental conditions. Calculating the theoretical OCV by the Nernst equation (Eq. (2)) helps to account for the slight difference of the OCVs (Table 2). The theoretical OCVs are almost the same each other for the given temperatures and oxygen partial pressures. The measured OCVs are also almost the same each other, but lower than the theoretical

Table 2
Theoretical open-circuit voltage (*V*)

	800 °C	900 °C
H_2–air fuel cell	1.10	1.08
H_2–O_2 fuel cell	1.13	1.12

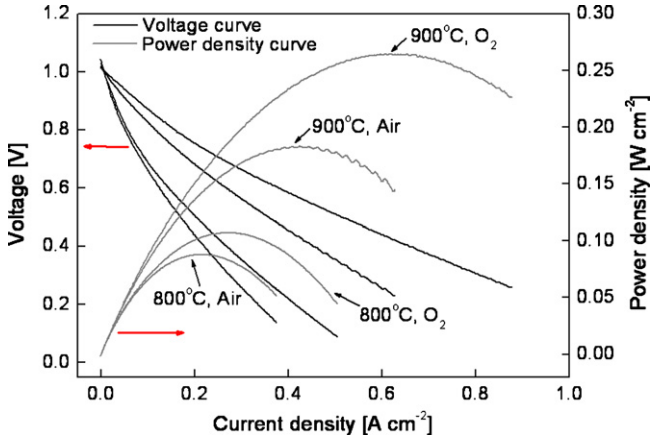

Fig. 8. *I–V–P* curves of single-cell vs. temperature and oxygen partial pressure.

OCVs. The lower OCV values may be caused by sealing problems. The influence of oxygen partial pressure and temperature on OCV is small in the range of the experimental conditions. Cell performances are improved by 50% by changing the oxygen partial pressure from the 0.21 atm of air to 1 atm. This is because the oxygen reduction reaction at the cathode is enhanced. The oxygen partial pressure dependence of the single-cell performance was also analyzed by the impedance measurements (Fig. 9). The impedance at 800 °C is slightly smaller than that in Fig. 5 because the cathode property is enhanced by in situ sintering with time. The impedances in the frequency range of 1–100 Hz region are mainly changed by the oxygen partial pressure. It is known that oxygen ionization is the rate-determining step of the oxygen reduction reaction, according to the oxygen partial pressure dependence of the impedance for the LSCM-8246 cathode [19]. The reciprocal of the impedance in the frequency region is proportional to the oxygen partial pressure, calculated from Fig. 9, raised to 0.4 power. This is in agreement with a reaction order of 3/8 [19].

4.3. Numerical analysis

A two-dimensional *x–y* Cartesian coordinate system was adopted to conduct the numerical calculation. The boundaries for the calculation were determined by the cross-section (A–A′) of the single-cell from Fig. 1 (Fig. 10). There are actually two different porous media, namely, the anode layer and the cermet adhesive layer. It is considered that the anode with smaller pores is the major cause of the concentration polarization loss,

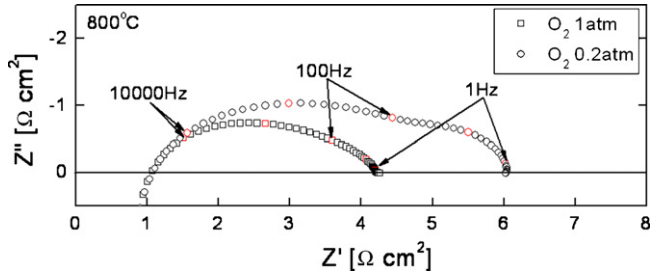

Fig. 9. Impedance spectra of single-cell vs. oxygen partial pressure at 800 °C.

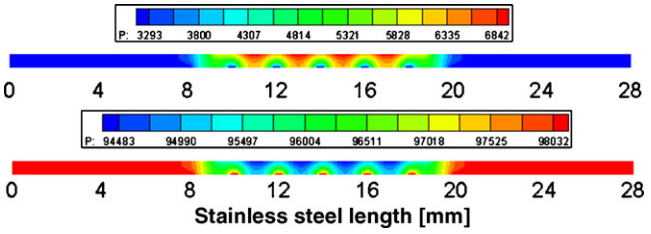

Fig. 10. Pressure gradients of water vapour (top) and hydrogen (bottom) at anode at 0.7 V at 800 °C.

neglecting the effect of the cermet adhesive layer. Knudsen diffusion can be ignored in the cermet adhesive layer because the pore size is so great that the Knudsen number can be smaller than 0.14, which is the critical value for the viscous diffusion regime from the Knudsen experiment [25]. Knudsen diffusion becomes important in the anode because the pore size is small. Furthermore, Knudsen diffusivity is much smaller (∼two orders of magnitude) than the binary diffusivity in the anode, implying that the gas diffusion is governed by Knudsen diffusion. Therefore, it can be assumed that the concentration change along the gas flow channel is negligible. The electrical current is consumed at the centre of the upper surface with an area of 1 cm^2. The reactant and product gases are fed from 11 holes, with 0.4 mm channel width, at the lower surface. The remainder of the surface is assumed to be blocked, not allowing any flow. The partial pressures of the gases are mainly distributed around the centre of the cell to generate the current. It can be shown that the water vapour production is comparable with the hydrogen consumption.

The *I–V* curve from numerical analysis is compared with the experimental data (Fig. 11). The trends of the curves are similar, but a large error exists in the low-current region. This is because the activation polarization loss is somewhat overestimated by the numerical calculations. The reaction order of 3/8 strongly affects the cell performance because the oxygen partial pressure dependence between the numerical and experimental results is similar. Each polarization loss has been calculated to investigate its contribution to the overall cell performance (Fig. 12). It is found that the activation polarization loss of the cathode provides

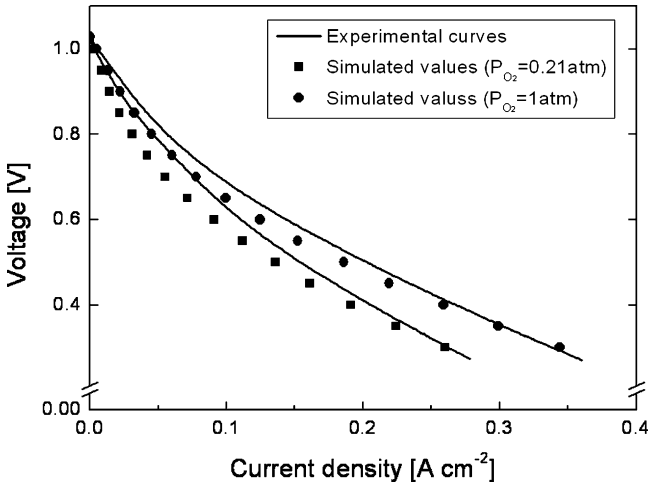

Fig. 11. Comparison between experimental *I–V* curves and simulated *I–V* curves for different oxygen partial pressures at 800 °C.

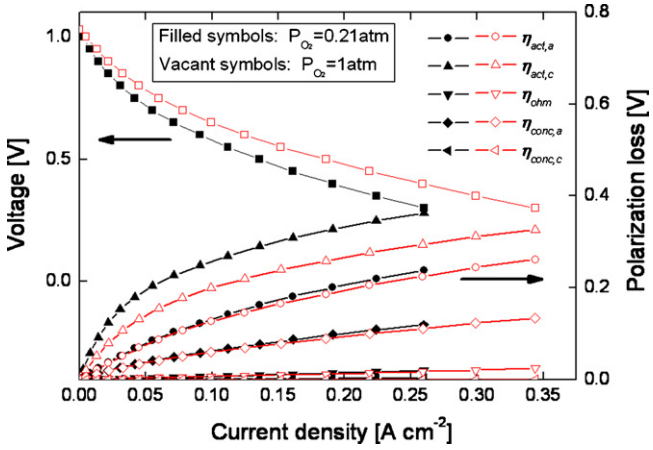

Fig. 12. Oxygen partial pressure dependence of polarization losses at 800 °C.

the largest contribution, whereas the concentration polarization loss of the cathode is very small. The activation polarization loss of the cathode decreases greatly with increasing oxygen pressure, whereas the other losses are only slightly decreased. The oxygen reduction reaction of the cathode is the dominant governing factor of the single-cell performance, compared with the impedance results of Fig. 9.

5. Conclusions

The area-specific resistance of a LSCM cathode on a YSZ electrolyte is measured. LSCM-8246 has the lowest ASR value because of the optimization of the oxygen reduction reaction kinetics, thermal expansion compatibility, and chemical reactivity. The impedance of an in situ sintered cathode is two orders of magnitude larger than the impedance of a cathode that is sintered at 1200 °C. A metal-supported SOFC single-cell is made by using a joining process to reduce the fabrication costs. Commercial STS430 is used as the metal support with the dimensions of 28 mm diameter, 1 mm thickness, and 0.4 mm channel width. The effects of temperature, oxygen partial pressure, and current collection by the pastes are investigated. The cell performance is influenced by the thermally activated process and the maximum power densities are 0.03, 0.09, and 0.18 W cm^{-2} at 700, 800, and 900 °C, respectively. Higher oxygen partial pressures elevate cell performance because the oxygen reduction reaction at the cathode is enhanced. The cell performance can also be improved by enhancing current collection with Ni paste at the anode and Pt paste at the cathode. Experimental and numerical analysis both conclude that the oxygen reduction reaction of the cathode dominates the overall cell performance.

Acknowledgements

This work is an outcome of the projects of the Best Lab Program of the Ministry of Commerce, Industry and Energy (MOCIE), and the Brain Korea 21 (BK21) Program of the Ministry of Education and Human Resources Development (MOE). The authors greatly appreciate financial support from these two sources.

References

[1] A. Baker, P. Bance, N. Brandon, B. Girvan, Proceedings of the Fuel Cell Seminar; Progress Challenges and Markets: Abstracts, Palm Spring, USA, 2005, pp. 49–52.
[2] N. Brandon, D. Corcoran, D. Cummins, A. Duckett, K. El-Khoury, D. Haigh, R. Leah, G. Lewis, N. Maynard, T. McColm, R. Trezona, A. Selcuk, M. Schmidt, J. Mater. Eng. Perform. 13 (2004) 253–256.
[3] R.T. Leah, N.P. Brandon, P. Aguiar, J. Power Sources 145 (2005) 336–352.
[4] J.-M. Bae, B.C.H. Steele, Solid State Ionics 106 (1998) 247–253.
[5] S.P. Yoon, J. Han, S.W. Nam, T.-H. Lim, I.-H. Oh, S.-A. Hong, Y.-S. Yoo, H.C. Lim, J. Power Sources 106 (2002) 160–166.
[6] J.-H. Koh, Y.-S. Yoo, J.-W. Park, H.C. Lim, Solid State Ionics 149 (2002) 157–166.
[7] J. Larminie, A. Dicks, Fuel Cell Systems Explained, second ed., John Wiley and Sons, 2003, pp. 48–53.
[8] S.H. Chan, K.A. Khor, Z.T. Xia, J. Power Sources 93 (2001) 130–140.
[9] A.V. Akkaya, Int. J. Energy Res. 31 (2007) 79–98.
[10] J.H. Nam, D.H. Jeon, Electrochim. Acta 51 (2006) 3446–3460.
[11] A. Weber, R. Darling, J. Meyers, J. Newman, Handbook of Fuel Cells, vol. 1, John Wiley and Sons, 2003, pp. 47–69.
[12] R.C. Reid, J.M. Prausnitz, B.E. Poling, The Properties of Gases and Liquids, fourth ed., McGraw-Hill, New York, 1987.
[13] B. Todd, J.B. Young, J. Power Sources 110 (2002) 186–200.
[14] S. Campanari, P. Iora, J. Power Sources 132 (2004) 113–126.
[15] B. Kenney, K. Karan, Solid State Ionics 178 (2007) 297–306.
[16] P. Costamagna, A. Selimovic, M. Del Borghi, G. Agnew, Chem. Eng. J. 102 (2004) 61–69.
[17] S. Campanari, P. Iora, Fuel Cells 5 (2005) 34–51.
[18] M.M. Hussain, X. Li, I. Dincer, Int. J. Energy Res. 29 (2005) 1083–1101.
[19] C. Lee, S.-W. Baek, J. Bae, Proceedings of the 16th International Conference on Solid State Ionics, Shanghai, China, 2007, p. P489.
[20] F.S. Baumann, J. Fleig, M. Konuma, U. Starke, H.-U. Habermeier, J. Maier, J. Electrochem. Soc. 152 (2005) A2074–A2079.
[21] V.A.C. Haanappel, A. Mai, J. Mertens, Solid State Ionics 177 (2006) 2033–2037.
[22] C. Lee, J. Bae, Trans. KSME B 30 (2006) 1211–1217 (in Korean).
[23] J.H. Yu, G.W. Park, S. Lee, S.K. Woo, J. Power Sources 163 (2007) 926–932.
[24] H. Ullmann, N. Trofimenko, F. Tietz, D. Stöver, A. Ahmad-Khanlou, Solid State Ionics 138 (2000) 79–90.
[25] M. Kaviany, Principles of Heat Transfer in Porous Media, second ed., Springer-Verlag, New York, 1995, pp. 365–390.